Structural controls on the hydrology of crevasses on the Greenland ice sheet

T. R. Chudley[1], P. Christoffersen [1], S. H. Doyle[2], T. P. F. Dowling[3], R. Law[1], C. M. Schoonman[1], M. Bougamont[1], B. Hubbard[2]

[1]Scott Polar Research Institute, University of Cambridge
[2]Centre for Glaciology, Department of Geography and Earth Sciences, Aberystwyth University
[3]Department of Geography, King's College London

Key Points:

- Crevasses on the Greenland Ice Sheet are observed to be water-filled when the mean normal stress is compressive and empty when extensional.
- Water-filled crevasses deliver water to the bed via episodic hydrofracture. Empty crevasses discharge water englacially and inefficiently.
- These two states, controlled by the surface stress regime, have distinct dynamic and thermal influences on ice sheets.

Corresponding author: Tom Chudley, `trc33@cam.ac.uk`

Abstract

Surface crevasses on the Greenland Ice Sheet deliver significant volumes of meltwater to the englacial and subglacial environment, but the topic has received little attention compared to supraglacial lake and moulin drainage. Here, we explore relationships between crevasse hydrology and the surface stress regime at a fast-flowing, marine-terminating sector of the Greenland ice sheet. Regional-scale observations of surface water, crevasses, and stress were made across a 3,000 km^2 region using satellite data. Contemporaneous high spatio-temporal resolution observations were obtained from uncrewed aerial vehicle surveys on Store Glacier using a supervised classifier and feature-tracked velocities. While previous studies have identified crevasses using von Mises stress thresholds, we find these are insufficient for predicting crevasse hydrology. We found that dry crevasse fields, where no ponded meltwater was observed through the entire melt season, were more likely to exist in tensile mean stress regimes, which we interpret to be due to meltwater draining continuously into the englacial system. Conversely, wet crevasse fields, hosting ponded meltwater, were more likely to exist in compressive mean stress regimes, which we interpret to be a result of closed englacial conduits. We show that these ponded crevasses drain through episodic rapid drainage events (i.e. hydrofracture). Mean stress regime can therefore inform spatially heterogeneous styles of meltwater delivery through crevasses to the bed of ice sheets, with distinct consequences for basal processes such as subglacial drainage efficiency and cryo-hydrologic warming. Thus, we recommend simple guidelines for improving the representation of crevasse hydrology in regional hydrological models.

1 Introduction

Surface crevasses are open fractures in glaciers and ice sheets, ranging in width from millimetres to tens of metres. As a visible expression of glacier stress regimes, the size and orientation of crevasses are closely linked to glacier dynamics, associated with extensional flow and deformation of ice through compression or shear along margins (Colgan et al., 2016). Motivations for detecting crevasses and understanding their formation include morphological insights into glacier flow (E. Phillips et al., 2013; Dell et al., 2019), the development of fracturing criteria for supraglacial lake drainage (Das et al., 2008; Arnold et al., 2014) and ice calving (Benn et al., 2017; Todd et al., 2019), and quantifying the dynamic influence of water transmitted to the bed of glaciers (McGrath et al., 2011; Koziol & Arnold, 2018).

In regions of high advection, such as fast-flowing outlet glaciers of the Greenland Ice Sheet (GrIS), crevasses form in upstream zones where extensional tensile stress regimes favour crevasse opening, and then advect downstream into regions where compressive stress regimes result in crevasse closure, forming healed crevasses. The fracture process is generally understood in terms of simple 1-D numerical models, such as the 'zero stress' model in which crevasses penetrate to the depth at which ice creep closure (due to ice overburden pressure) equals tensile stress (Nye, 1957), or the linear elastic fracture mechanics (LEFM) approach, which further accounts for factors such as stress concentrations at fracture tips, fracture toughness, geometry, and water level (van der Veen, 1998; Krawczynski et al., 2009). There is a growing recognition of the need to understand more complex multidimensional and mixed-mode crevasse formation (Colgan et al., 2016), but transferring mechanical understanding to higher dimensions is nontrivial (van der Veen, 1999; Colgan et al., 2016). As such, many studies that predict crevasse presence in real-world scenarios use simpler methods such as basic thresholds of first principal strain or von Mises Stress (Poinar et al., 2015; Clason et al., 2015; Koziol et al., 2017; Williamson, Willis, et al., 2018), which have been identified from observational studies to be suitable predictors of crevasse presence (Vaughan, 1993; Hambrey & Müller, 1978; Harper et al., 1998; van der Veen, 1998).

Crevassing is an important mechanism to transfer water to the bed of the GrIS and water itself drives the propagation of crevasses via hydrofracture (Weertman, 1973; R. B. Alley et al., 2005; van der Veen, 2007; Krawczynski et al., 2009). Once full-depth hydrofracture has occurred, water flow forms an efficient route for continued meltwater delivery to the bed in the form of moulins. To date, this meltwater pathway to the bed has largely been focussed on supraglacial lake drainage (Banwell et al., 2016; Hoffman et al., 2018; Christoffersen et al., 2018). Crevasse hydrology has been included in only a few recent numerical modelling studies (e.g. Clason et al., 2015; Koziol et al., 2017; Koziol & Arnold, 2018)), but is understood to capture as much as half of seasonal surface runoff (McGrath et al., 2011; Koziol et al., 2017). Despite the apparent importance of crevasse hydrology, there are few studies of the transfer of water to the bed of ice masses through crevasse fields, and the limited number of studies that do exist describe variable - and often contradictory - processes. Some studies observe discrete drainage of crevasses (Lampkin et al., 2013; Cavanagh et al., 2017), which appear to result from episodic full-depth hydrofracture and display similarities to supraglacial lake drainages. In contrast, other studies conceptualise crevasse fields as continuously, but inefficiently, transmitting a low water flux to the subglacial system without the need for full-depth hydrofracture (Colgan et al., 2011; McGrath et al., 2011). However, no studies have attempted to account for this spectrum of observations and the assumptions surrounding crevasse hydrology, nor attempted to explain where and why these types of drainage occur. Given this lack of information, previous modelling studies have assumed that crevasse drainage occurs in a uniform manner, and use existing thresholds intended to predict crevasse presence to instead predict crevasse hydrology (Clason et al., 2015; Everett et al., 2016; Koziol et al., 2017). To date, no observational studies exist to guide such choices.

This study aims to better understand crevasse hydrological behaviour by relating the presence of crevasses and water to stress regimes in the ablation zone of the GrIS at two different spatial scales. The first utilises large-scale, satellite-derived data to examine crevasses in a ~3000 km^2 sector of west Greenland, including five major marine-terminating outlet glaciers . The second uses high-resolution photogrammetric datasets collected by uncrewed aerial vehicles (UAVs) to closely examine crevasses in a 7 km^2 area of fast glacier flow within this sector, allowing us to validate large-scale data and record processes occurring at the scale of individual crevasses. Our goal is to understand how glacier dynamics relate to the spectrum of observed crevasse hydrology, and thereby develop guidelines to allow hydrological models to account for the heterogeneity of crevasse hydrological behaviour.

2 Methods

2.1 Study area

We assess satellite-derived data over a ~3000 km^2 sector of the western GrIS (Figure 1), extending ~90 km from Sermeq Kujalleq (Danish/English: Store Glacier; 70.4°N 50.6°W) in the south to Perlerfiup Sermia (71.0°N, -50.9°W) in the north. Within this large-scale region of interest (the 'satellite ROI'), we use UAV surveys and Structure-from-Motion with Multi-View Stereo (SfM-MVS) photogrammetry to assess, at high resolution, a crevasse field in the Store Glacier drainage basin, 25 km from the calving front (the 'UAV ROI'). The UAV ROI is 1.5 km wide and 5 km long, and was chosen based on its coverage of an initiating crevasse field, ranging from areas with no visible crevasses to areas with crevasses greater than 50 m wide.

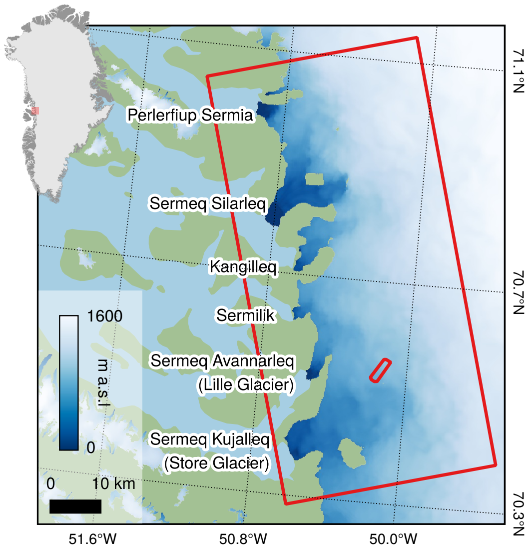

Figure 1. Map of study region. Small red box outline indicates the extent of UAV surveys. Large red box outlines the extent of satellite image analysis. Marine-terminating outlet glaciers are labelled, with the Danish/English name in brackets where applicable. Surface elevation shown in colour is from ArcticDEM v3 (Porter et al., 2018).

2.2 Satellite data

2.2.1 Crevasse classification

A binary crevasse mask (Figure 2) of the satellite ROI was produced from ArcticDEM v3 mosaic data at 2 m resolution (Porter et al., 2018). Crevasse identification from digital elevation models can be approached in a variety of ways (Florinsky & Bliakharskii, 2019), but we use a simple method identifying crevasses from the residuals between the original and a smoothed elevation model. As a result, we limit our analysis to the outer 40 km of the ablation zone (Figure 1), where snow-filled crevasses are rare, in order to reduce the number of false negatives in the final dataset. We performed these operations in Google Earth Engine (GEE; Gorelick et al., 2017), which allows for efficient computation and rapid evaluation over a large study area. We first cropped the ArcticDEM to the GIMP ice mask (Howat et al., 2014), before smoothing the elevation model by convolving the raster with a circular kernel of 50 m radius. Residuals greater than 1 m between the smoothed and raw elevation values were identified as crevasses. To compare with stress estimates, the 2 m dataset was aggregated into grid cells to match the resolution (200 m) and projection (NSIDC sea ice polar stereographic north) of the velocity grid. Aggregated values ranged from 0–1, representing the fraction of grid cell area classified as crevasses.

Because relict crevasses can advect through a variety of stress regimes (Mottram & Benn, 2009), we further identified crevasse initiation zones. We manually identified the upstream boundary between crevasse fields and bare ice from the 2 m crevasse dataset. Then, we used a 200 m buffer to identify pixels in the 200 m dataset that should be classified as being in crevasse initiation zones.

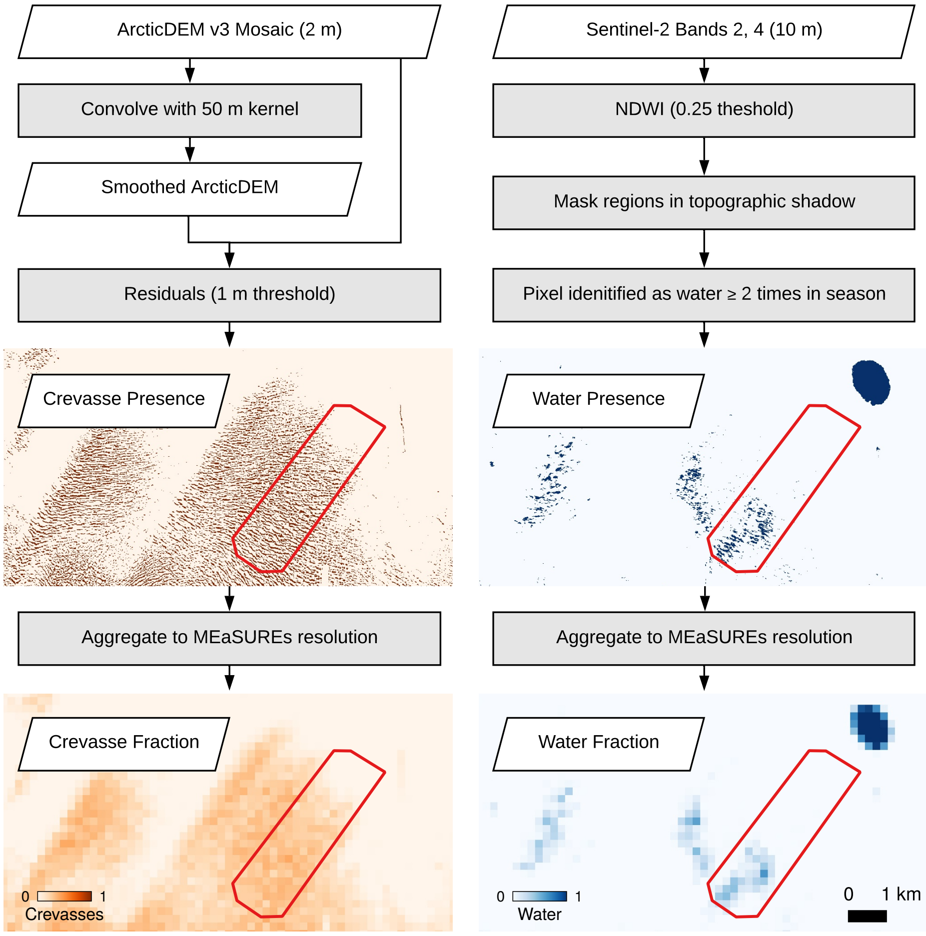

Figure 2. Flow diagram visualising the production of crevasse fraction data from ArcticDEM (left) and water fraction data from Sentinel-2 optical imagery (right). Red box outlined in maps marks the extent of the UAV ROI.

2.2.2 Water classification

We produced a binary map of water presence across the satellite ROI through the 2018 melt season (Figure 2) using Sentinel-2 imagery in GEE. The ablation season of 2018 was chosen for analysis to match the timing of the UAV surveys on Store Glacier. We first identified all Sentinel-2 scenes with $< 40\%$ cloud cover and $< 70°$solar zenith angle between May-October 2018, selecting a total of 360 images. We clipped the images to the GIMP ice mask (Howat et al., 2014) and converted digital number values to top of atmosphere (TOA) reflectance. TOA reflectance values have been shown to be suitable for identifying surface water in Greenland with Landsat 8 OLI imagery (Pope, 2016), and have been used for surface water classification in Sentinel-2 data (Williamson, Banwell, et al., 2018). We then calculate the normalised difference water index (NDWI) from bands 2 (blue) and 4 (red) for all images: following Williamson, Banwell, et al. (2018) for the Store Glacier region, we use an NDWI threshold of 0.25 to create binary water classification maps for each Sentinel-2 image. In order to avoid false positive identification of shaded regions, we mask areas in topographic shadow with the GEE hillShadow function, using the ArcticDEM for topography and the solar zenith angle from Sentinel-2 image metadata. Finally, we sum the image stack to count the number of times through the 2018 melt season that a pixel was identified as water. In order to reduce the chance of false positive classification (e.g. cloud shadow, ephemeral slush zones at the beginning of the melt season) we classify as water any pixel that was identified as water in ≥ 2 images through the melt season. As for crevasse maps, we aggregate this data onto the velocity grid with a unit of fractional coverage of water within each grid cell.

2.2.3 Stress classification

Although some previous studies have used strain rate thresholds to predict crevasse location (Poinar et al., 2015; Williamson, Willis, et al., 2018), we follow the recommendations of Colgan et al. (2016) to use estimated stress thresholds as a robust and generalisable criterion across glaciers of widely varying thermal regimes. Studies exploring relationships between crevassing, hydrology, and surface dynamics have used a multitude of 2-D stress measures. In order to test this variation, we calculate: (i) the first and second principal stresses (σ_1 and σ_2 as applied by Poinar et al. (2015) and Williamson, Willis, et al. (2018); (ii) the longitudinal stress (σ_l; as used by Clason et al. 2015); and (iii) the von Mises yield stress (σ_v; as used by Clason et al., 2015; Koziol et al., 2017; Everett et al., 2016). We were also motivated to test further measures of stress, as σ_1, σ_2, and σ_l consider stress in only one axis, whilst σ_v considers only the deviatoric component of the stress tensor. Hence, we calculated the mean stress (σ_m, also referred to as the hydrostatic stress), and the signed von Mises Stress (σ_{sv}). Both of these measures account for the normal components of the stress tensor.

Stresses were estimated using surface strain derived from MEaSUREs (Making Earth System Data Records for Use in Research Environments) gridded GrIS velocity data for 2018 (Joughin et al., 2010), with Glen's flow law as the constitutive equation following Clason et al. (2015). We first calculated the surface strain rate tensor $\dot{\epsilon}_{ij}$ from the horizontal components of velocity u and v (in grid directions x and y):

$$\dot{\epsilon}_{ij} = \begin{bmatrix} \frac{\delta u}{\delta x} & \frac{1}{2}(\frac{\delta v}{\delta x} + \frac{\delta u}{\delta y}) \\ \frac{1}{2}(\frac{\delta v}{\delta x} + \frac{\delta u}{\delta y}) & \frac{\delta v}{\delta y} \end{bmatrix} = \begin{bmatrix} \dot{\epsilon}_x & \dot{\epsilon}_{xy} \\ \dot{\epsilon}_{xy} & \dot{\epsilon}_y \end{bmatrix} \tag{1}$$

We approximated the derivatives using the finite difference of the velocity field (K. E. Alley et al., 2018). We calculated longitudinal strain rate ($\dot{\epsilon}_l$) by resolving strain-rate components relative to the local flow direction according to Bindschadler et al. (1996):

$$\dot{\epsilon}_l = \dot{\epsilon}_x \cos^2\alpha + 2\dot{\epsilon}_{xy} \sin\alpha + \dot{\epsilon}_y \sin^2\alpha \tag{2}$$

where α is the flow angle defined anti-clockwise from the x axis. Stresses approximated from strain rates following Nye (1957):

$$\sigma_{ij} = B\dot{\epsilon}_e^{(1-n)/n}\dot{\epsilon}_{ij} \tag{3}$$

Where $\dot{\epsilon}_e$ is effective strain, calculated following Cuffey and Paterson (2010):

$$\dot{\epsilon}_e = \sqrt{\frac{1}{2}[\dot{\epsilon}_{xx} + \dot{\epsilon}_{yy}] + \dot{\epsilon}_{xy}} \tag{4}$$

and n is the flow law exponent with value 3. B is a viscosity parameter, which we follow Clason et al. (2015) in assigning a value of 324 kPa a$^{1/3}$ (based on an assumed ice temperature of -5 °C).

The first principal stress (σ_1) was calculated as the highest eigenvalue of the stress tensor σ_{ij}, and second principal stress (σ_2) as the lowest eigenvalue (Jouvet et al., 2017).

We calculate the von Mises yield criterion (σ_v) according to Vaughan (1993):

$$\sigma_v = \sqrt{(\sigma_1\sigma_1) + (\sigma_2\sigma_2) - (\sigma_1\sigma_2)} \tag{5}$$

We calculate the mean stress (σ_m) as follows:

$$\sigma_m = \frac{1}{2}[\sigma_1 + \sigma_2] \tag{6}$$

Finally, the signed von Mises stress (σ_{sv}) is a simple modification of the von Mises stress, calculated as the magnitude of σ_v with the sign of σ_m:

$$\sigma_{sv} = \mathrm{sgn}(\sigma_M) \cdot \sigma_V \tag{7}$$

2.3 UAV data

2.3.1 UAV photogrammetry and velocity

We acquired aerial imagery across a 13-day period in July 2018 (Table S1) utilising a custom-built, fixed-wing UAV with 2.1 m wing span. Imagery was collected using a Sony *alpha*6000 24 MP camera with a fixed 16-mm lens, processed using Structure-from-Motion with Multi-View Stereo (SfM-MVS) photogrammetry, and used to derive velocity fields within the UAV ROI as described by Chudley, Christoffersen, Doyle, Abellan, and Snooke (2019). In brief, photogrammetry was performed using AgiSoft Metashape v.1.4.3 software, and geolocated by using an on-board L1 carrier-phase GPS unit (post-processed against an on-ice ground station) to locate the position of aerial photos. Outputs from the photogrammetric process were 0.15 m resolution orthophotos and 0.2 m DEMs. Horizontal velocity fields were derived by feature-tracking topographic hillshades using OpenPIV (Taylor et al., 2010). Stress fields were derived as outlined in Section 2.2.3, with a 5 x 5 pixel median-filter on the input velocity fields introduced as an additional preprocessing step to reduce noise.

2.3.2 Surface classification

To date, UAV-based crevasse detection has been based on DEM-based topographic analysis (Ryan et al., 2015; Florinsky & Bliakharskii, 2019). Whilst these methods have been shown to be useful from a hazard assessment perspective (Florinsky & Bliakharskii,

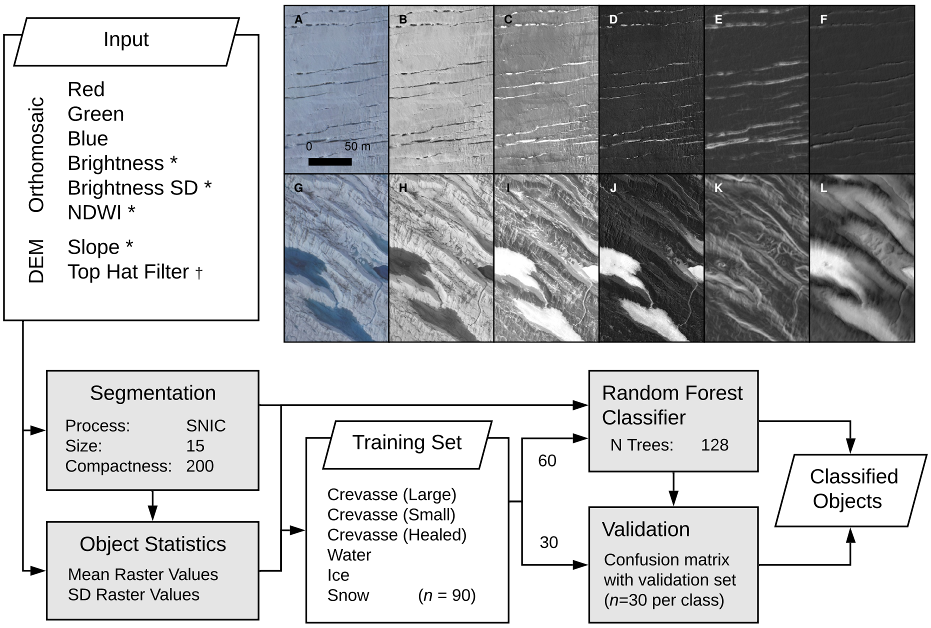

Figure 3. Flowchart of method used to classify UAV imagery. Variables appended with an asterisk were calculated from input data within GEE, while those appended with a cross were calculated separately in Matlab. Inset shows examples of OBIA input data for regions dominated by small (a-f) and (g-l) large crevasses. (a and g) RGB orthophotos. (b and h) Brightness. (c and i) Standard deviation of RGB values. (d and j) NDWI. (e and k) Slope, with hillshade overlaid. (f and l) Black-top-hat filtered DEM, with hillshade overlaid.

2019), DEM-based methods alone cannot be used to identify features such as water-filled or healed crevasses, and crevasse detection is sensitive to threshold choice and ultimately the resolution of the DEM (Jones et al., 2018; Florinsky & Bliakharskii, 2019). To take advantage of the high spatial resolution and multi-dimensional outputs of UAV surveys, we used a combination of object-based image analysis (OBIA) and supervised classification. OBIA is based not on the numerical characteristics of individual pixels but of objects (i.e. groups of meaningfully similar pixels segmented based upon spectral homogeneity) (Blaschke, 2010)). This has been used successfully in a glaciological context by Kraaijenbrink et al. (2016, 2018) for mapping cliff/pond systems and emissivity on a debris-covered glacier. We again used GEE to perform the full segmentation and supervised classification workflow (Figure 3).

We identified a number of variables that could be used as inputs for a supervised classification algorithm to identify crevasse field surface features. This included: the red, blue, and green values of the orthophoto (Figure 3a;g); the 'brightness' (mean RGB values; Fig 3b;h) as per Kraaijenbrink et al. (2016); the standard deviation of the RGB values, which appeared to highlight water, small crevasses, and healed crevasses (Figure 3c;i); the NDWI, from blue and red pixel values (Figure 3d;j); the DEM slope, which effectively highlighted small crevasses on the order of a few metres (Figure 3e;k); and DEM values black-top-hat filtered with a 30 m structuring element (Kodde et al., 2007), which were useful in identifying large crevasses on the order of tens of metres (Figure 3f;l). A black top-hat filter morphologically closes the glacier surface at scales smaller than the structuring element, before subtracting the closed surface from the original data. This process was performed in Matlab prior to ingestion into GEE.

We performed image segmentation using Simple Non-Iterative Clustering (SNIC) (Achanta & Susstrunk, 2017), a computationally efficient implementation of superpixel-based clustering. Rather than segmenting an image into semantically-meaningful objects, superpixel-based segmentation simplifies the image into small, uniform, and compact clusters of similar pixels ('superpixels'), with a focus on boundary adherence. The variables described above are used as the input to the segmentation algorithm. We manually selected a seed spacing of 15 pixels (2.25 m) and a high compactness factor of 200. This resulted in superpixels small enough to display strong boundary adherence to small and healed crevasses at the scale of metres, whilst still clearly delineating the margins of larger features such as water bodies. As an input to the supervised classification, we calculated the average and standard deviation of values in each superpixel from the variables described above, as well as the perimeter-to-area ratio of the superpixel, and normalised the results.

We adopted a supervised classification approach to surface classification (Kraaijenbrink et al., 2016, 2018; Ryan et al., 2018) by training a random forest classifier in GEE. In order to reduce the amount of redundant information used to train the random forest classifier, we performed a non-parametric mutual information (MI) test on our training data as a proxy for the predictive power of each input variable. Rejecting input variables beneath the median MI value (Figure S1) did not notably reduce the accuracy of the output data (Figure S2). Therefore, we used only the nine most significant variables as input to the random forest classifier. We constructed training datasets of 90 points each for six distinct surface types: bare ice, snow, healed crevasses, 'small' crevasses, 'large' crevasses, and water. We seperated 'small' and 'large' crevasses (those with a diameter of metres vs. tens of metres) into two training datasets as they displayed distinctly different values for properties such as brightness, slope, and the top hat filtered DEM (Figure 3). We trained the random forest classifier on two-thirds of the dataset (60 points per classification) and retained one-third (30 points per classification) for validation. Output classification performed well visually (Figure S3) and validation data showed that a $> 95\%$ accuracy was observed for all surface types (Figure S2), apart from for snow and bare ice, which for our purposes was not important. Although we identified six surface types, for this analysis we were only interested in three distinctions: crevasses (combining 'small' and 'large' crevasses), ice (combining bare ice, snow, and healed crevasses), and water.

3 Results

3.1 Satellite results

From ArcticDEM elevation, Sentinel-2 optical imagery, and MEaSUREs surface velocity (Figure 4a), we created maps of crevasse fraction values (Figure 4b), water fraction values (Figure 4c), and stress estimates (Figure 4d–i) respectively.

Despite an intuitive relationship between first principal stress (σ_1) (Figure 4d; 5a) and crevasse formation, the measure is not a good predictor of crevasse state, i.e. whether a crevasse is initiating, dry, or wet. An analysis of the distribution of stresses shows that although all crevasse types occur at higher values of σ_1 than non-crevassed regions (Figure 6a), the three states display similar median values (wet 47 kPa; dry 48 kP; initiating 50 kPa), suggesting that σ_1 alone is not a strong control on crevasse hydrology. In contrast, second principal stress (σ_2; Figure 4e) displays a clearer relationship with crevasse state, with crevasses initiating in areas of highest σ_2 and ponding in areas of lowest σ_2 (Figure 5b). Initiating crevasses have the highest median σ_2 (-13 kPa) and are the most common crevasse state in regions of positive σ_2 (Figure 6b). In contrast, wet crevasses have the lowest median σ_2 (-58 kPa), and dry crevasses are intermediate between the two (-38 kPa). Longitudinal stress (σ_l; Figure 4f), is more successful at distinguishing crevasse state (Fig 5C; median wet 6 kPa; dry 18 kPa; initiating 33 kPa) than σ_1, but not as successful as σ_2 as it displays a narrower spread of median values, and dry and wet crevasse states display very similar distributions (Figure 4c). The effective performance of σ_2, and less effective performance of σ_1 and σ_l, suggest that structural controls on crevasse hydrology are distinct from those traditionally understood to control crevasse formation.

Stress criteria that encompass both σ_1 and σ_2 provide further insights into crevasse hydrology. Von Mises (σ_v; Figure 4g; 5d) has different median values for crevasse states (wet 88 kPa, dry 67 kPa, initiating 57 kPa), but with a counter-intuitive relationship given that the highest stresses appear to be the most likely to be water-filled. Additionally, dry and wet crevasses display a strong positive skew (Figure 6d), making it difficult to differentiate the two based on a single threshold. In contrast, σ_m values (Figure 4h; 5e) capture a distribution for each of the crevasse states: crevasse initiation is most likely to occur at the highest σ_m values (median +20 kPa), whilst water-filled crevasses are the only surface type to occur with a median negative σ_m (-4 kPa). Qualitative assessment (Figure 4e) shows that saturated crevasse zones align with regions of negative σ_m and crevasse initiation zones align with strongly positive σ_m. However, σ_m is still not convenient for predicting crevasse state as the distributions of crevasse states display high overlap (Figure 6e) such that simple thresholding based on σ_m alone would not delineate crevasse state successfully.

In order to combine the relative strengths of σ_v and σ_m approaches, we use σ_{sv} which is derived as the magnitude of σ_v but with the sign of σ_m (Figure 4i). This measure allows for a more refined differentiation for whether a stress regime is compressive or extensional. Crevasse initiation zones display a particularly narrow distribution (Figure 6f) almost exclusively in positive σ_{sv} regimes (median +57 kPa). Wet and dry crevasses can also be differentiated, even though these data exhibit a similarly skewed distribution in σ_v. When σ_{sv} is highly compressional (i.e., less than -50 kPa), wet crevasses are more likely than dry crevasses; above this value, the probability of crevasse state is approximately equal. Conversely, dry crevasses are more likely than wet crevasses to exist in extensional σ_{sv} regimes from low to high stress (up to 120 kPa). In very high pos-

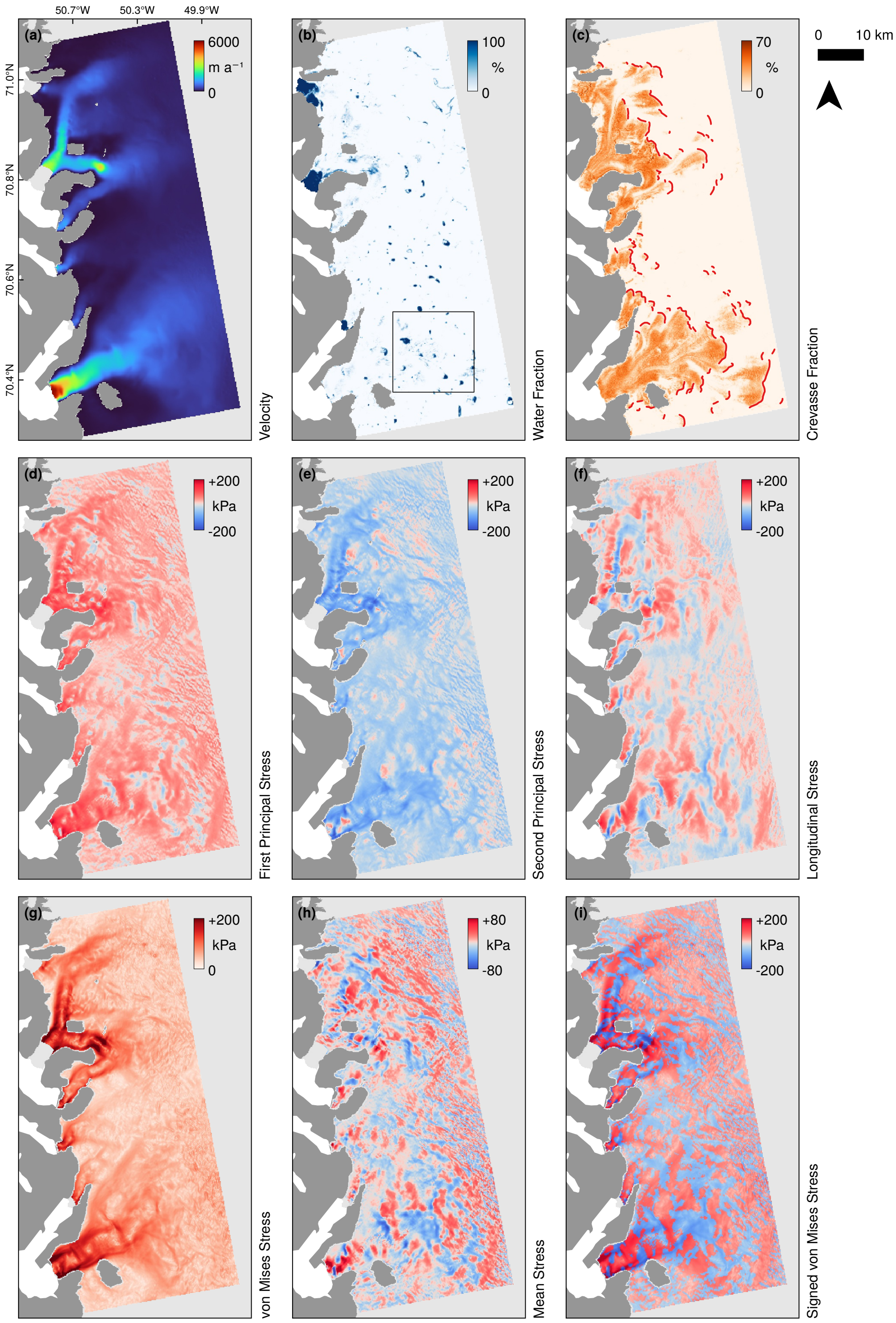

Figure 4. (a) Map of MEaSUREs 2018 velocity data over the study region; (b) observed 2018 water fraction; (c) observed crevasse coverage, with manually identified crevasse initiation zones marked in red; (d) first principal stress, (e) second principal stress, (f) longitudinal stress; (g) von Mises Stress, (h) mean stress, and (i) signed von Mises Stress. Black box in (b) shows the location of Figure 5.

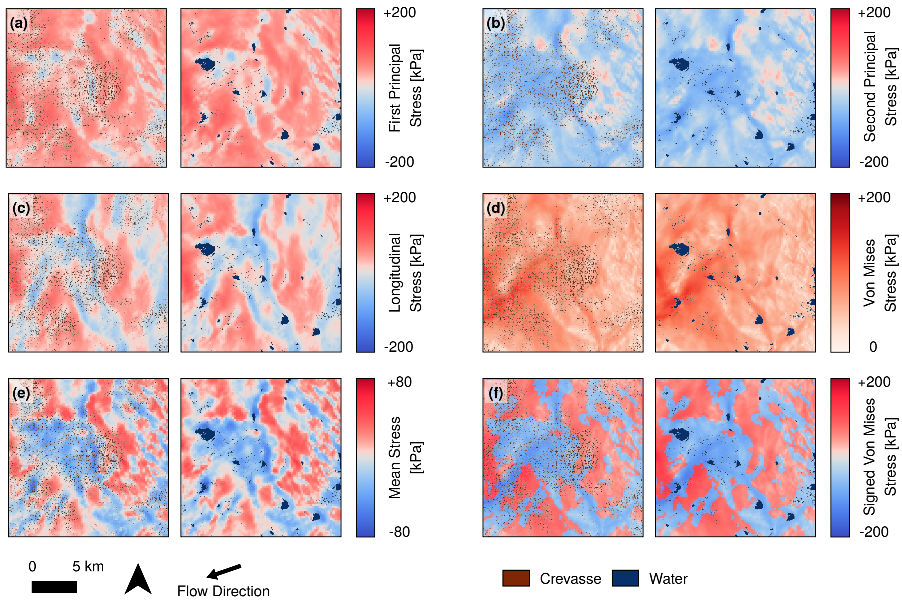

Figure 5. Close-up of stress fields overlaid with observed crevasses (left) and water (right): (a) first principal stress, (b) second principal stress, (c) longitudinal stress; (d) von Mises Stress, (e) mean stress, and (f) signed von Mises Stress.

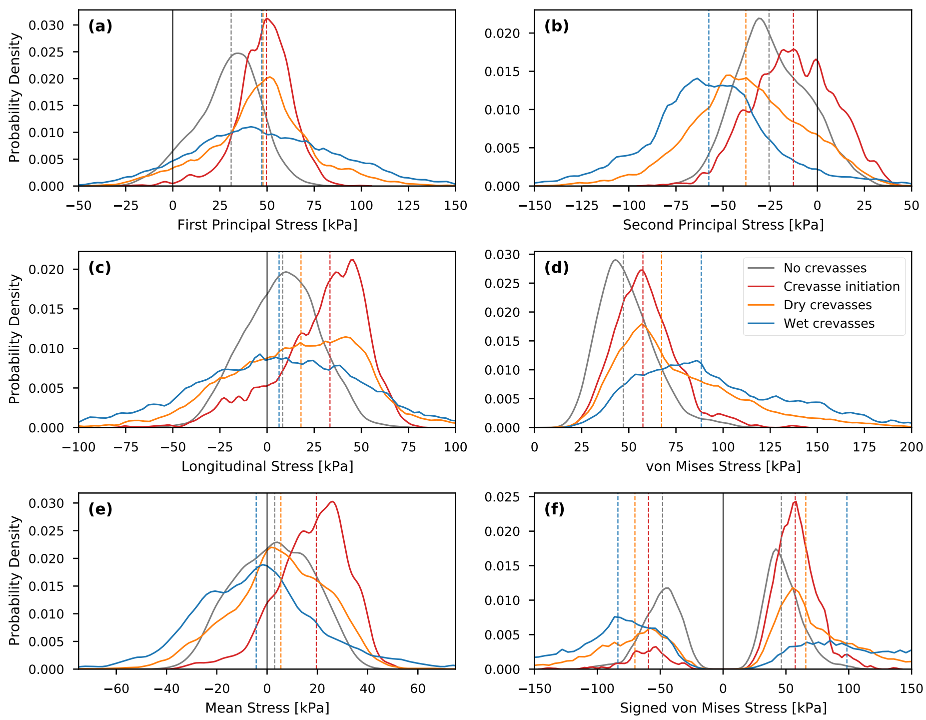

Figure 6. Kernel density estimate distribution plots of different surface classifications for (a) first principal stress, (b) second principal stress, (c) longitudinal stress, (d) von Mises stress, (e) mean stress, and (f) signed von Mises Stress. Median values for different surface classifications are shown as dashed vertical lines. A crevassed grid cell is defined by > 1% crevasse fraction, and a wet crevassed grid cell is a crevassed grid cell with any water observed (> 0%).

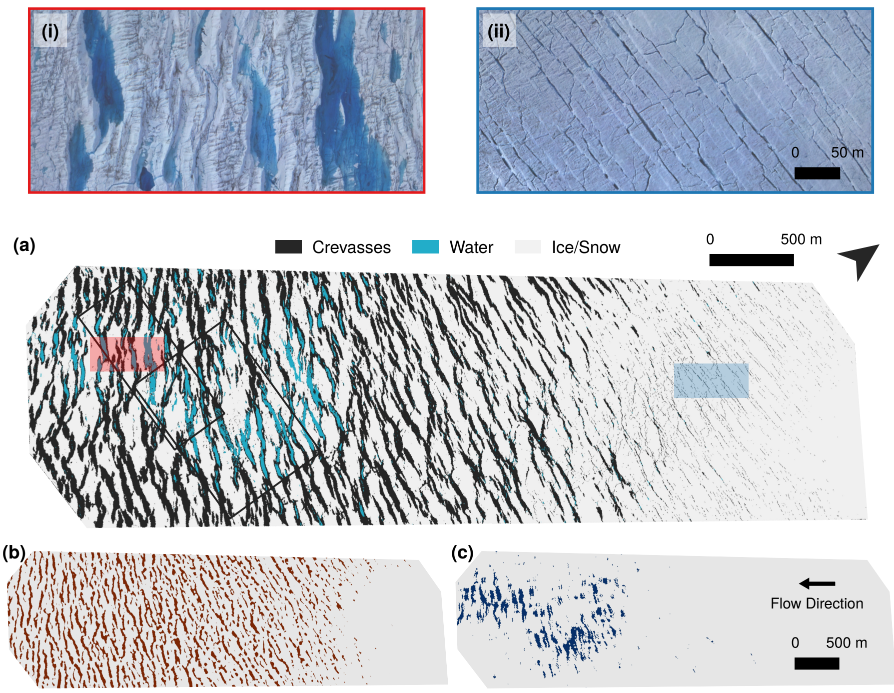

Figure 7. Output of (a) UAV random forest classification, with insets (shaded in red and blue) showing (i) an area with large (50-60 m) crevasses, and (ii) small (2-3 m) crevasses. Satellite-derived data, shown for comparison, include (b) ArcticDEM-derived crevasse classification, and (c) Sentinel-2 derived water classification. Black boxes in (a) mark extents of Figure 9.

itive σ_{sv} regimes (greater than 120 kPa), wet crevasses are once again more likely to exist.

3.2 UAV results

3.2.1 Analysis and comparison to satellite data

UAV surface classification (Figure 7a), based on high resolution orthophotos (0.15 m) and DEMs (0.2 m), was able to differentiate crevasses, water, and ice surfaces to a level of accuracy exceeding 90% (Figure S2). This suggests that the UAV SfM-MVS is highly suitable as ground verification for the coarser satellite-derived data, especially given the logistical difficulties of ground-based verification within hazardous crevasse fields. Comparison with satellite-derived crevasse classification (Figure 7b) and water classification (Figure 7c) shows that the datasets agree closely in terms of the distribution of surface features. Manual comparison between the two datasets suggests the cutoff width below which crevasses are unable to be identified from ArcticDEM v3 data is approximately 10 m , corresponding to 5 pixels. Although this means the satellite data do not capture the smallest crevasse fields, the resolvable size of a crevasse is approximately equal to the resolution of the Sentinel-2 bands used for NDWI calculation (10 m), which gives confidence that the two datasets are comparable. While our ArcticDEM mosaic is derived from multitemporal data (individual tiles across the study area range from 2009-2017), crevasse sizes and patterning observed in 2018 UAV surveys were consistent with the 2009-2017 ArcticDEM (Figure 7a cf. 6b). This suggests that, even though individual crevasses

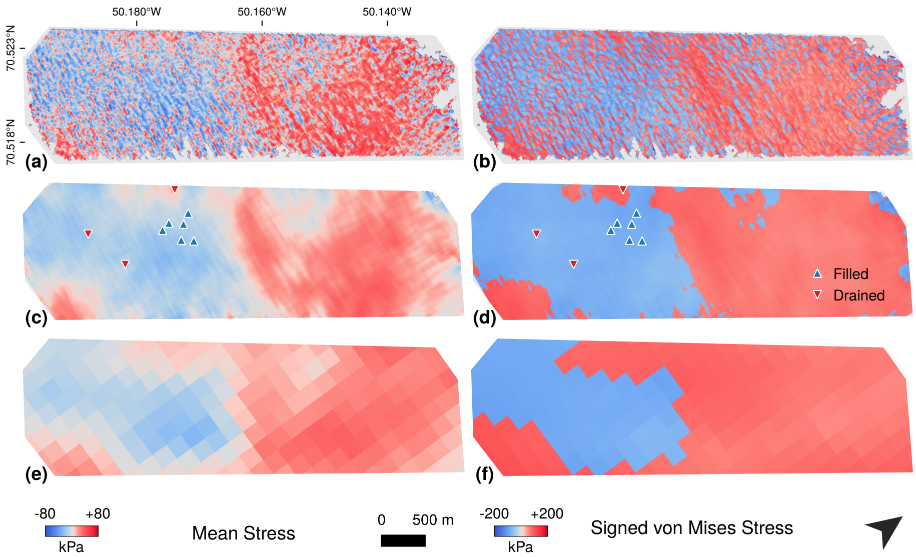

Figure 8. UAV-derived stress outputs for mean stress (left column) and signed von Mises stress (right column). (a–b) shows raw output, (c–d) shows 200 m mean average, and (e–f) shows MEaSUREs-derived output for comparison. Triangles in (c–d) show the locations of crevasse systems that were observed to fill (blue) or drain (red) across the UAV survey period.

advect, interannual variation in crevasse fields is relatively small, and that the assumption that 2009-2017 crevasse distribution can be compared to 2018 surface water distribution is valid. Sentinel-2 water and UAV-derived water also agree (Figure 7a cf. 6c). Individual water-filled crevasses are able to be co-located between the satellite and UAV datasets. Sentinel-2 data additionally identifies additional crevasses that are water-filled across the span of the season yet not filled on the date of the UAV survey.

Stress components evaluated from UAV velocity data, including σ_m (Figure 8a) and σ_{sv} (Figure 8b), reveal a highly heterogeneous stress regime, where changes can be seen even between neighbouring crevasses. However, in general, an extensional regime dominates in the northeast (right-hand side of Figures 6 and 7) and a compressive regime in the southwest. As with satellite-derived data, there are clear relationships between the nature of the positive/negative mean stress regime and that of crevasse initiation and water distribution. Crevasses tend to initiate - or at least become identifiable in the decimetre resolution data - in the upstream kilometre of the study zone (Figure 7a). In the next kilometre down-glacier, crevasses open from $<$ 3 m wide to full size ($\sim$10–60 m wide) by the centre of the study zone (Figure 7a insets). Crevasse initiation and opening is coincident with a zone of highly positive mean stress, consistent with satellite-derived observations (Section 3.1). In the southwestern sector of the study zone, crevasse size remains relatively stable, but crevasses transition from dry to water-filled in the down-glacier direction (Figure 7a). This region of water-filled crevasses is seen where the mean stress regime is negative (Figure 8a–b), which is again consistent with satellite datasets.

The stress regime as estimated from UAV-derived velocity fields is highly variable on the scale of tens of metres, making it difficult to compare to the stress regime estimated from MEaSUREs data. To address this, we apply a 31 pixel (198.4 m) mean filter across the UAV stress fields (Figure 8c–d) to approximate the 200 m resolution of the MEaSUREs stress field (Figure 8e–f). The results show that the UAV and MEaSUREs data are in close general agreement, despite the different spatial resolution (6.4 m vs 200

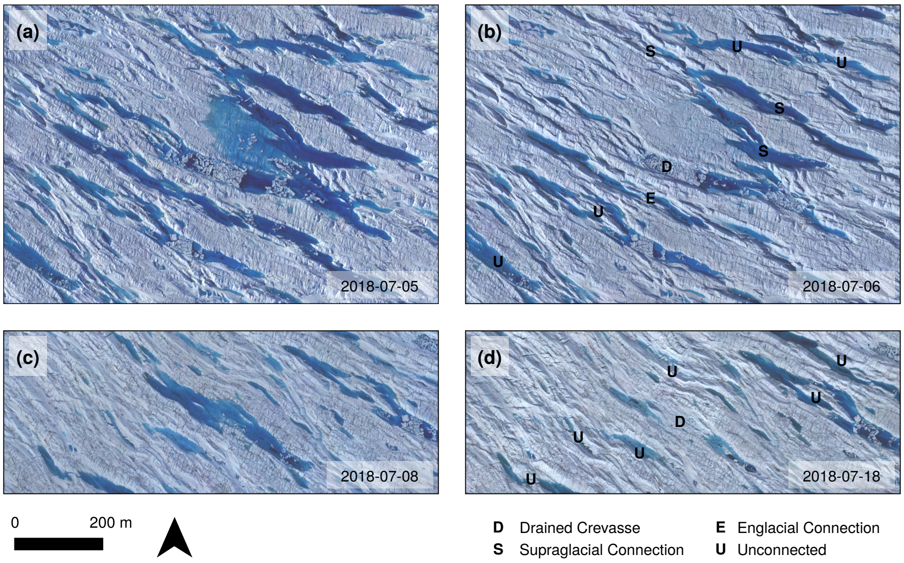

Figure 9. Examples of crevasse drainage when (a–b) a draining crevasse is supraglacially and/or englacially connected to adjacent crevasses and (c–d) when no connections are present. Interpretations are marked where crevasses underwent direct drainage (D), drained via supraglacial connection to a draining crevasse (S), drained via englacial connection to a draining crevasse (E), or remained unconnected to a draining system (U).

m) and timescales over which velocity was captured (10 days vs 1 year composite). This reveals that crevasse fields exhibit high local variability in surface stresses (on the scale of 10s of metres) that cannot be captured by satellite observations. For instance, in the southwestern sector of the study zone, there are many localised areas of positive stress, despite the fact that MEaSUREs data is consistently negative. This suggests that one source of uncertainty in the satellite analysis is the degree to which localised variability occurs within its 200 m grid cells.

3.2.2 Water routing in ponded crevasse fields

Satellite-derived analysis (Section 3.1) identified regions of wet crevasses in compressive mean stress regimes, but did not provide information as to whether or how water is routed to the bed in these areas. Over the 13-day period in July 2018 over which repeat UAV surveys were undertaken (Table S1), three crevasse systems in the UAV ROI were observed to drain, and six underwent significant filling. The locations of these events are correlated with mean stress regime (Figure 8c–d). For instance, crevasse water filling was observed in a region that had recently advected from a net extensional into a net compressive zone. Elsewhere, crevasse drainage was observed in a region that had recently advected from a net compressive area (where $\sigma_m < 0$) into a net extensional area ($\sigma_m > 0$), and also in locations where the 200 m-resolution stresses were observed to be negative but local stresses displayed high heterogeneity (cf. Figure 8a–b; c–d). This suggests that, in general, crevasses fill with water when advecting into a negative mean stress regime, and display a higher propensity to drain when advecting into a region of positive mean stresses.

Closer analysis of these draining crevasses revealed two key observations regarding water routing. First, there was little evidence to suggest that surface water was routed for significant distances between crevasses in crevasse fields. Where supraglacial streams existed, connecting larger crevasses, they were easily identified in the imagery (Figure S4a), but this is not common across the survey zone. In one case, a crevasse system that was overflowing with water (Figure 9a) formed local supraglacial networks, and upon one crevasse draining, water levels across the entire network dropped (Figure 9b). This event appeared to result in the formation of incised channels in the days following drainage (Figure S4b–c). It was less common for adjacent crevasses to drain when no surface routing was visible (Figure 9b), and indeed individual crevasses were able to drain without affecting water levels in the surrounding crevasses at all (Figure 9c–d). This suggests that supraglacial and englacial hydrological connections between crevasses may be rare. Second, crevasse drainages appear to be rapid. Of the three drainages we identified, two represent crevasses that were stable or filling in sequential imagery prior to drainage, before losing a majority of water between two adjacent images (e.g. Figure 9c–d). One crevasse system lost a substantial volume of water in less than 24 hours (Figure 9a–b), and water levels continued to drop for the rest of the survey period (Figure S4b–c). This suggests that either a moulin had formed, and that water therefore continued to drain into the subglacial system, or that small open fractures continued to transfer water inefficiently into the englacial system.

4 Discussion

4.1 Relationships between surface stress and observed crevasse hydrology

Our findings show that stress measures previously used to predict water drainage through crevasses - including the first principal stress (Poinar et al., 2015; Williamson, Willis, et al., 2018), longitudinal stress (Clason et al., 2015), and von Mises stress (Koziol et al., 2017; Everett et al., 2016) – are not good at estimating the hydrological state of crevasses. Longitudinal stress (σ_l) is effective at predicting where crevasses initiate, which aligns with the assertion that crevasses can be considered as Mode I fractures that open up perpendicular to the direction of flow when stress in this direction exceeds a certain threshold. However, the fact that both first principal stress (σ_1) and σ_l are poor at predicting crevasse hydrology, whilst second principal stress (σ_2) performs better, suggests that the full range of normal stress, and not only the stress acting in the direction of flow, affect the ability of water to drain englacially. The von Mises (σ_v) criterion, which accounts for only the deviatoric stress, does not clearly distinguish crevasse hydrological state compared to alternative measures which incorporate the full first invariant stress (e.g. mean stress). Additionally, σ_v displays an inverse relationship to hydrology, whereby higher σ_v values are more likely to see water ponding occur (Figure 6d). This is counterintuitive when considering σ_v as a planform equivalent to a σ_{xx} in an LEFM framework, where high positive σ_{xx} values (tensile stress) are associated with greater fracture propagation (van der Veen, 1998). We suggest this is because the von Mises stress does not differentiate between a compressive or extensional stress regime. In contrast, stress measures that account for the magnitude and direction of the full first invariant stress (i.e. mean stress, σ_m, and signed von Mises stress, σ_{sv}) were better at predicting surface crevasse hydrology. Surface crevasses that were identified to be water-filled through the 2018 ablation season were more likely to exist in regions where mean surface stress was negative (i.e. compressive). In contrast, surface crevasses where no water was observed were more likely to exist in positive (i.e. extensional) mean stress regimes. To explain this link, we interpret that in negative mean stress regimes, hydrological pathways between the surface and active englacial system will likely be subject to enhanced closure. This will be the case regardless of the stress acting in the direction perpendicular to crevasse orientation (Section 4.2.1).

There has been limited consideration of the role of the full first invariant stress in crevasse hydrology, with most studies focussed on first principal or longitudinal stress.

A few studies have considered the role of σ_2 in crevasse formation (Hambrey & Müller, 1978; Cuffey & Paterson, 2010), and indirectly in studies of Mode II (van der Veen, 1999) and Mode III (Colgan et al., 2016) shear in mixed-mode crevasse formation. Whilst LEFM modelling can, in theory, be extrapolated to two or even three dimensions (van der Veen, 1999), this is nontrivial (Colgan et al., 2016). As a result, studies modelling water transmission to the bed have tended to extrapolate from 1-D LEFM models by directly replacing the σ_{xx} stress term with pre-existing measures that have been recommended for crevasse formation - in particular, the von Mises stress, following Vaughan (1993). Our work suggests that this can be improved upon, and that accounting for crevasse hydrology requires a more complete consideration of stresses, i.e. both surface-parallel principal stresses.

4.2 Crevasse drainage mechanisms

4.2.1 Wet crevasses

A number of drainage processes could be consistent with observations of water-filled crevasses. For instance, water-filled crevasses in compressive regions can be part of an active supraglacial network, with water being routed to a moulin elsewhere in the system (Poinar, 2015). However, the UAV data presented here suggests that, where crevasses are large, significant hydrological connections between them are rare and of limited spatial extent (Figure 9b,d). Even where hydrological connections exist, they appear to form as a consequence, rather than a cause, of drainage events (Figure S4b–c). If channels do not exist in many cases, the drainage of water in ponded crevasse systems cannot, for the most part, be caused by water being routed to moulins via supraglacial networks.

Given that we found little direct evidence for hydrological connections, we consider hydrofracture to the subglacial environment to be the most likely mechanism by which water-filled crevasses drain (Weertman, 1973; Boon & Sharp, 2003; van der Veen, 2007; Krawczynski et al., 2009). In negative mean stress regimes, we assume that englacial connections undergo what Irvine-Fynn et al. (2011) described as 'pinch-off', whereby crevasse closure or ice creep can isolate the ponded crevasse from the englacial drainage system. In an environment where ablation is ongoing, this will result in the filling of surface crevasses, allowing hydrofracture to occur when water depth reaches a critical level. This would be consistent with the rapid and heterogenous crevasse drainages observed in UAV data, and align with the numerous observations of hydrofracture occurring during rapid lake drainages (Das et al., 2008; Doyle et al., 2013; Stevens et al., 2015; Chudley, Christoffersen, Doyle, Bougamont, et al., 2019).

The state of a subglacial drainage system and subsequent ice dynamic response is known to be affected by the variability (Schoof, 2010) and distribution (Banwell et al., 2016) of meltwater inputs. Our evidence indicates that episodic crevasse drainage events should be expected to deliver distinct, isolated pulses of meltwater to the bed in the same fashion as - but likely smaller than - rapid lake drainages. The full hydrological consequences of rapid lake drainages are explored in detail elsewhere (e.g. Nienow et al., 2017)), but it is apparent that similar principles can be applied to crevasse drainages. For instance, studies focussing on draining crevasse systems at the shear margin of Jakobshavn Isbrae have established that water delivery is of sufficient volume to overwhelm the capacity of the subglacial system (Lampkin et al., 2013), increasing ice mass flux across the shear margin and enhancing glacier discharge (Cavanagh et al., 2017; Lampkin et al., 2018). However, there may be several features of crevasse drainages that are distinct from better-studied lake drainage events. After hydrofracture, ongoing meltwater delivery via the newly open moulin is an important hydrological component of lake drainages (Koziol et al., 2017; Hoffman et al., 2018) but, given the smaller catchments that individual crevasses have, this effect is likely less important in crevasse drainage scenarios. Unlike lakes, it appears to be relatively common that crevasse systems can drain multiple times through a single ablation season (Cavanagh et al., 2017). However, the net effect of this has yet to be properly considered.

4.2.2 Dry crevasses

As water is never observed to pond in the crevasses we classify as 'dry', surface meltwater produced within the crevasse catchment must either (i) drain via moulins to the glacier bed, or (ii) drain less efficiently into the englacial system, but still rapidly enough that water is never collecting at a rate sufficient to fill the crevasse. We argue that the second interpretation is more likely. Whilst it seems unlikely that discharge rates are sufficient to maintain open moulins, positive mean stress regimes may mean that, unlike in compressive environments, creep closure does not close narrow hydrological pathways to the englacial system. This is consistent with the view of crevasse systems on temperate valley glaciers as continually, albeit inefficiently, hydraulically connected to englacial and/or subglacial drainage systems through a linked network of small fractures (Fountain et al., 2005).

This conceptual model of inefficient, continuous crevasse drainage has previously been applied to the Greenland Ice Sheet by Colgan et al. (2011) and McGrath et al. (2011). Both studies assumed that water reaches the bed, albeit slower than through moulins. Colgan et al. (2011) suggested the difference may be 200-fold between the two types of surface-to-bed connection ($\sim$1 hour for a 1 m^2 moulin vs. $\sim$12 hours for a 0.1 m wide crevasse), whilst McGrath et al. (2011) suggested that crevasses may slow englacial drainage to such an extent that a diurnal cycle of meltwater input can be damped to a quasi-steady-state discharge on the timescale of hours-days. This sustained inefficient delivery of meltwater to the glacier bed through crevasses would be less likely to overwhelm the transmission capacity of the subglacial system. Therefore, they argue that regions of the bed subject to continuous inefficient delivery are less likely to exhibit enhanced basal sliding compared to regions experiencing episodic, efficient meltwater pulses.

There is no direct evidence, however, that water draining inefficiently through crevasses is able to reach the bed of the Greenland Ice Sheet. Another likelihood is that much of this water does not make it to the bed, and instead freezes englacially. This has consequences for the thermal structure of glaciers, as it has been argued that widespread, inefficient meltwater delivery through open crevasses would facilitate cryo-hydrologic warming relative to regions fed by discrete moulins (Colgan et al., 2011). This is because a dense spacing of hydrological pathways increases the volume of ice warmed by the latent heat release of englacial freezing, and hence can act to enhance ice velocity via deformation (T. Phillips et al., 2010; Lüthi et al., 2015). In contrast, episodically-draining, water-filled crevasses may focus cryo-hydrologic warming into the upper few hundred metres of the ice column (Poinar, 2015), and open moulins provide little latent heat to the surrounding ice (Lüthi et al., 2015). As such, it is likely that crevasses that drain continuously into the ice sheet may act to enhance latent heat delivery relative to other hydrological pathways. Colgan et al. (2011) concluded that increased crevasse coverage on an accelerating ice sheet would increase the area of the bed experiencing enhanced cryo-hydrologic warming. Based on the findings presented here, it might be expected that an accelerating ice sheet would result in a transition of some crevassesed regions from episodic to continuous drainage if the mean stress were to become positive (extensional). If this is the case, some areas of the bed could experience a transition to enhanced cryo-hydrologic warming, even in regions where crevasse fields already existed.

4.3 Implications for large-scale ice sheet modelling

Neither of the two states of crevasse drainage described above is new, with both episodic full-depth hydrofracture and continuous englacial drainage having numerous examples of observations and model implementations in literature focusing on the Green-

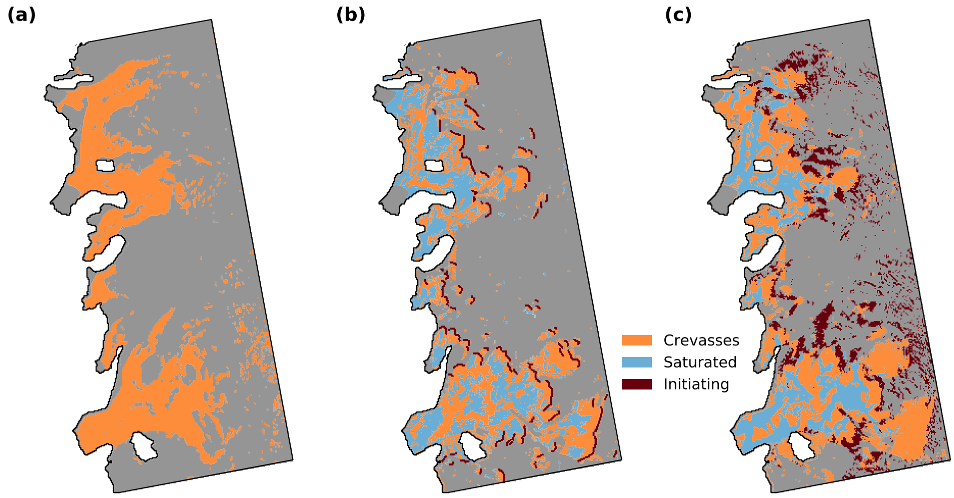

Figure 10. Comparisons of methods of using stress thresholds to identify crevassing. (a) Predicted distribution of crevassing using a von Mises yield threshold of 67.5 kPa. (b) Observed distribution of crevasse-filled pixels (crevasse fraction > 1%) , crevasse-filled pixels where water is observed , and manually identified crevasse initiation zones. (c) Predicted location of water-filled crevasses and crevasse initiation zones based on signed von Mises thresholds.

land Ice Sheet. Nevertheless, in the past, regional models of ice sheet hydrology and dynamics have rarely included crevasse drainage (Arnold et al., 2014; Banwell et al., 2013, 2016). Recent 2-D regional hydrological models have begun to include the process, but have yet to account for heterogeneous drainage styles. Clason et al. (2015) incorporated crevasse drainage in a manner similar to the episodic hydrofracture described above. They identified crevassed regions based on a σ_v threshold, which were then allowed to fill and hydrofracture according to an LEFM model (van der Veen, 2007). Once a crevasse fractured to the full ice thickness, a moulin formed and water was transferred continuously to the bed. More recently, Koziol et al. (2017) based their model on the principle of continuously draining crevasses, whereby meltwater produced at the surface of crevasse fields (again identified according to a σ_v threshold) drained immediately without requiring hydrofracture. This water was assumed to reach the bed of the ice sheet without freezing englacially. These two studies, reflecting a paucity of observations, assumed that all crevasse drainage falls into one of the end-members of crevasse hydrology observed and described herein.

Given the above, we are able to use the findings of this study to provide recommendations as to how future studies may be able to account for a wider diversity of crevasse hydrology whilst keeping inputs and classifications as simple as possible. We compare our results to the common method of crevasse field prediction via a qualitatively identified von Mises stress threshold. A threshold yield strength of 67.5 kPa was determined to result in the best visual match between predicted (Figure 10a) and observed (Figure 10b) crevasse fields. This method provides a reasonable first-order estimate but is (i) poor at predicting marginal cases including zones of false negative results in regions of relict crevasses, and (ii) cannot distinguish between zones of episodic and continuous drainage as identified in this study. Accepting that zero stress models cannot account for relict crevasse advection (Mottram & Benn, 2009), we retain the use of our own direct observations rather than using stress thresholds to predict crevasse location (Figure 10c). This is achievable for future studies as the method we use is simple and relies only on ArcticDEM data. Then, based upon the stress distribution of surface types (Figure 6f) and visual matching with observed distribution (Figure 10b), we prescribe that water-filled crevasses exist in MEaSUREs grid cells where σ_{sv} is less than -65 kPa or greater than +140 kPa (Figure 10c). On a pixel-by-pixel level, these thresholds are able to predict the presence or absence of water in 63% of crevassed grid cells correctly. Visual comparison shows that this thresholding technique provides a good match with broad trends in crevasse ponding. This includes the diagonal band of ponding across the tongue of Store Glacier, a bias of ponding towards the shear margins of the northern tributary of Perlerfiup Sermia, and even some of the specific localised patterns further upstream into the drainage basin at Store Glacier. This suggests that simple thresholding such as this could be used as input to regional hydrological models to investigate the seasonal and long-term effects of spatial heterogeneity in crevasse hydrology on the subglacial dynamics of the ice sheet (see, for example, Poinar et al., 2019).

In another example of implementing signed Von Mises stress as an improved simple stress threshold, we use the distribution of stresses in manually identified crevasse initiation zones (Figure 4e) to prescribe a yield criterion of +55 kPa for crevasse initiation (Figure 10c). This falls within the 30-90 kPa bounds predicted by (van der Veen, 1998), but is lower than the 67.5 kPa we prescribed for von Mises stress alone, as well as those thresholds used by other studies (e.g. Clason et al., 2015; Koziol et al., 2017). By using a directional measure of stress, a relatively low critical yield criterion can be prescribed without enhancing regions of false positive identification in compressive stress regimes. Initiation zones are clustered where anticipated, at the upstream margins of crevasse fields, which gives us confidence in this threshold. There also exist scattered initiation zones at the farthest inland regions of the study area, where crevasses are not observed in our ArcticDEM-derived dataset. However, examination of higher-resolution Sentinel-2 data reveals that there are visible crevasse features here, not identified within the study due to either being too small to appear in ArcticDEM data or snow-filled.

The regional observations presented in this study utilise bulk analysis of annual velocity and seasonal water presence to identify potential links between crevasse hydrology and stress regime. Future work should explore opportunities to better define this relationship using time-series datasets. For example, the proliferation of remote sensing platforms has allowed for the production of ice velocity datasets at extremely high temporal resolutions (e.g. Minchew et al., 2017), as well as the ability to track the filling and drainage of individual hydrological systems on the surface of ice sheets (Williamson, Banwell, et al., 2018). These advances highlight the possibility of being able to relate the behaviour and drainage of crevasses with time-variable stress regimes induced by short-term instabilities in ice dynamics - as has been previously proposed from a modelling perspective for supraglacial lake drainage events (Christoffersen et al., 2018) - and hence provide new insights into the relationship between crevasses and the delivery of meltwater to the bed of ice sheets.

5 Conclusions

In order to be able to model and predict the response of GrIS dynamics to increasing runoff, it is necessary to understand where and how water is transferred to the bed of the ice sheet. Our results indicate that surface stresses, and in particular the mean normal stress, determines whether crevasses drain episodically via hydrofracture, influencing basal sliding, or drain inefficiently into the englacial system, enhancing cryo-hydrologic warming via refreezing. Our observations suggest that crevasse drainage state exists on a spectrum that is controlled by spatially heterogeneous surface stress. We find that these behaviours cannot be distinguished based upon the yield criterion previously used to predict crevasse distribution, suggesting that controls on crevasse hydrology are distinct from controls on crevasse initiation. Simple thresholds obtained from visual analysis remain, however, a suitable approach to predict the first-order distribution of crevasse hydrological state. Hence, we can recommend mean stress thresholds as a simple and practical method for improving the representation of crevasse hydrology in regional hydrological models, which is necessary to be able to accurately model the spatially variable impact of seasonal ice sheet hydrology on the thermal regime and ice dynamic behaviour of the Greenland Ice Sheet.

Acknowledgments

This research was funded by the European Research Council as part of the RESPONDER project under the European Union's Horizon 2020 research and innovation program (Grant 683043). TRC and RL were supported by a Natural Environment Research Council Doctoral Training Partnership Studentship (Grant NE/L002507/1). We are very grateful to Ann Andreasen and the Uummannaq Polar Institute for their kind hospitality; to Sean Peters for his assistance with UAV launches; and to Neil Arnold for useful methodological discussions.

MEaSUREs annual velocity mosaics are available from the National Snow and Ice Data Centre (`https://doi.org/10.5067/OBXCG75U7540`). Sentinel-2 and ArcticDEM v3 data were made available for processing via Google Earth Engine. Data produced in this study will be made available via the UK Polar Data Centre (UK PDC) alongside the final publication of this manuscript.

The authors declare no financial conflict of interest.

References

Achanta, R., & Susstrunk, S. (2017). Superpixels and polygons using simple non-iterative clustering. In *Proceedings of the IEEE Conference on Computer Vision and Pattern Recognition* (pp. 4651–4660). doi: 10.1109/CVPR.2017.520

Alley, K. E., Scambos, T. A., Anderson, R. S., Rajaram, H., Pope, A., & Haran, T. M. (2018). Continent-wide estimates of Antarctic strain rates from Landsat 8-derived velocity grids. *Journal of Glaciology*, *64*(244), 321–332. doi: 10.1017/jog.2018.23

Alley, R. B., Dupont, T. K., Parizek, B. R., & Anandakrishnan, S. (2005). Access of surface meltwater to beds of sub-freezing glaciers: Preliminary insights. *Annals of Glaciology*, *40*, 8–14. doi: 10.3189/172756405781813483

Arnold, N. S., Banwell, A. F., & Willis, I. C. (2014). High-resolution modelling of the seasonal evolution of surface water storage on the Greenland Ice Sheet. *The Cryosphere*, *8*(4), 1149–1160. doi: 10.5194/tc-8-1149-2014

Banwell, A. F., Hewitt, I., Willis, I., & Arnold, N. (2016). Moulin density controls drainage development beneath the Greenland ice sheet. *J. Geophys. Res. Earth Surf.*, 2015JF003801. doi: 10.1002/2015JF003801

Banwell, A. F., Willis, I. C., & Arnold, N. S. (2013). Modeling subglacial water routing at Paakitsoq, W Greenland. *J. Geophys. Res. Earth Surf.*, *118*(3), 1282–1295. doi: 10.1002/jgrf.20093

Benn, D. I., Åström, J., Zwinger, T., Todd, J., Nick, F. M., Cook, S., ... Luckman, A. (2017). Melt-under-cutting and buoyancy-driven calving from tidewater glaciers: New insights from discrete element and continuum model simulations. *Journal of Glaciology*, *63*(240), 691–702. doi: 10.1017/jog.2017.41

Bindschadler, R., Vornberger, P., Blankenship, D., Scambos, T., & Jacobel, R. (1996). Surface velocity and mass balance of Ice Streams D and E, West Antarctica. *Journal of Glaciology*, *42*(142), 461–475. doi: 10.3189/S0022143000003452

Blaschke, T. (2010). Object based image analysis for remote sensing. *ISPRS Journal of Photogrammetry and Remote Sensing*, *65*(1), 2–16. doi: 10.1016/j.isprsjprs.2009.06.004

Boon, S., & Sharp, M. (2003). The role of hydrologically-driven ice fracture in drainage system evolution on an Arctic glacier. *Geophysical Research Letters*, *30*(18). doi: 10.1029/2003GL018034

Cavanagh, J. P., Lampkin, D. J., & Moon, T. (2017). Seasonal Variability in Regional Ice Flow Due to Meltwater Injection Into the Shear Margins of Jakobshavn Isbræ. *Journal of Geophysical Research: Earth Surface*, *122*(12), 2488–2505. doi: 10.1002/2016JF004187

Christoffersen, P., Bougamont, M., Hubbard, A., Doyle, S. H., Grigsby, S., & Pettersson, R. (2018). Cascading lake drainage on the Greenland Ice Sheet triggered by tensile shock and fracture. *Nature Communications*, *9*(1), 1064. doi: 10.1038/s41467-018-03420-8

Chudley, T. R., Christoffersen, P., Doyle, S. H., Abellan, A., & Snooke, N. (2019). High-accuracy UAV photogrammetry of ice sheet dynamics with no ground control. *The Cryosphere*, *13*(3), 955–968. doi: 10.5194/tc-13-955-2019

Chudley, T. R., Christoffersen, P., Doyle, S. H., Bougamont, M., Schoonman, C. M., Hubbard, B., & James, M. R. (2019). Supraglacial lake drainage at a fast-flowing greenlandic outlet glacier. *Proceedings of the National Academy of Sciences*, *116*(51), 25468–25477. doi: 10.1073/pnas.1913685116

Clason, C. C., Mair, D. W. F., Nienow, P. W., Bartholomew, I. D., Sole, A., Palmer, S., & Schwanghart, W. (2015). Modelling the transfer of supraglacial meltwater to the bed of Leverett Glacier, Southwest Greenland. *The Cryosphere*, *9*(1), 123–138. doi: 10.5194/tc-9-123-2015

Colgan, W., Rajaram, H., Abdalati, W., McCutchan, C., Mottram, R., Moussavi, M. S., & Grigsby, S. (2016). Glacier crevasses: Observations, models, and mass balance implications. *Reviews of Geophysics*, *54*(1), 119–161. doi: 10.1002/2015RG000504

Colgan, W., Steffen, K., McLamb, W. S., Abdalati, W., Rajaram, H., Motyka, R., … Anderson, R. (2011). An increase in crevasse extent, West Greenland: Hydrologic implications. *Geophysical Research Letters*, *38*(18). doi: 10.1029/2011GL048491

Cuffey, K. M., & Paterson, W. S. B. (2010). *The physics of glaciers.* Academic Press. doi: 10.1016/C2009-0-14802-X

Das, S. B., Joughin, I., Behn, M. D., Howat, I. M., King, M. A., Lizarralde, D., & Bhatia, M. P. (2008). Fracture Propagation to the Base of the Greenland Ice Sheet During Supraglacial Lake Drainage. *Science*, *320*(5877), 778–781. doi: 10.1126/science.1153360

Dell, R., Carr, R., Phillips, E., & Russell, A. J. (2019). Response of glacier flow and structure to proglacial lake development and climate at Fjallsjökull, south-east Iceland. *Journal of Glaciology*, 1–16. doi: 10.1017/jog.2019.18

Doyle, S. H., Hubbard, A. L., Dow, C. F., Jones, G. A., Fitzpatrick, A., Gusmeroli, A., … Box, J. E. (2013). Ice tectonic deformation during the rapid in situ drainage of a supraglacial lake on the Greenland Ice Sheet. *The Cryosphere*, *7*(1), 129–140. doi: 10.5194/tc-7-129-2013

Everett, A., Murray, T., Selmes, N., Rutt, I. C., Luckman, A., James, T. D., … Reeve, D. E. (2016). Annual down-glacier drainage of lakes and water-filled crevasses at Helheim Glacier, southeast Greenland. *Journal of Geophysical Research: Earth Surface*, *121*(10), 1819–1833. doi: 10.1002/2016JF003831

Florinsky, I. V., & Bliakharskii, D. P. (2019). Detection of crevasses by geomorphometric treatment of data from unmanned aerial surveys. *Remote Sensing Letters*, *10*(4), 323–332. doi: 10.1080/2150704X.2018.1552809

Fountain, A. G., Jacobel, R. W., Schlichting, R., & Jansson, P. (2005). Fractures as the main pathways of water flow in temperate glaciers. *Nature*, *433*(7026), 618–621. doi: 10.1038/nature03296

Gorelick, N., Hancher, M., Dixon, M., Ilyushchenko, S., Thau, D., & Moore, R. (2017). Google Earth Engine: Planetary-scale geospatial analysis for everyone.

Remote sensing of Environment, *202*, 18–27. doi: 10.1016/j.rse.2017.06.031

Hambrey, M. J., & Müller, F. (1978). Structures and ice deformation in the white glacier, Axel Heiberg Island, Northwest Territories, Canada. *Journal of Glaciology*, *20*(82), 41–66. doi: 10.3189/S0022143000021213

Harper, J. T., Humphrey, N. F., & Pfeffer, W. T. (1998). Crevasse patterns and the strain-rate tensor: A high-resolution comparison. *Journal of Glaciology*, *44*(146), 68–76. doi: 10.3189/S0022143000002367

Hoffman, M. J., Perego, M., Andrews, L. C., Price, S. F., Neumann, T. A., Johnson, J. V., ... Lüthi, M. P. (2018). Widespread Moulin Formation During Supraglacial Lake Drainages in Greenland. *Geophys. Res. Lett.*, 2017GL075659. doi: 10.1002/2017GL075659

Howat, I. M., Negrete, A., & Smith, B. E. (2014). The Greenland Ice Mapping Project (GIMP) land classification and surface elevation data sets. *The Cryosphere*, *8*(4), 1509–1518. doi: 10.5194/tc-8-1509-2014

Irvine-Fynn, T. D., Hodson, A. J., Moorman, B. J., Vatne, G., & Hubbard, A. L. (2011). Polythermal glacier hydrology: A review. *Reviews of Geophysics*, *49*(4). doi: 10.1029/2010RG000350

Jones, C., Ryan, J., Holt, T., & Hubbard, A. (2018). Structural glaciology of Isunguata Sermia, West Greenland. *Journal of Maps*, *14*(2), 517-527. doi: 10.1080/17445647.2018.1507952

Joughin, I., Smith, B. E., Howat, I. M., Scambos, T., & Moon, T. (2010). Greenland flow variability from ice-sheet-wide velocity mapping. *Journal of Glaciology*, *56*(197), 415–430. doi: 10.3189/002214310792447734

Jouvet, G., Weidmann, Y., Seguinot, J., Funk, M., Abe, T., Sakakibara, D., ... Sugiyama, S. (2017). Initiation of a major calving event on the Bowdoin Glacier captured by UAV photogrammetry. *The Cryosphere*, *11*(2), 911–921. doi: 10.5194/tc-11-911-2017

Kodde, M., Pfeifer, N., Gorte, B., Geist, T., & Höfle, B. (2007). Automatic glacier surface analysis from airborne laser scanning. *International Archives of the Photogrammetry, Remote Sensing and Spatial Information Sciences*, *36*(3/W52), 221–226.

Koziol, C. P., & Arnold, N. (2018). Modelling seasonal meltwater forcing of the velocity of land-terminating margins of the Greenland Ice Sheet. *The Cryosphere*, *12*(3), 971–991. doi: 10.5194/tc-12-971-2018

Koziol, C. P., Arnold, N., Pope, A., & Colgan, W. (2017). Quantifying supraglacial meltwater pathways in the Paakitsoq region, West Greenland. *Journal of Glaciology*, 1–13. doi: 10.1017/jog.2017.5

Kraaijenbrink, P. D. A., Shea, J. M., Litt, M., Steiner, J. F., Treichler, D., Koch, I., & Immerzeel, W. W. (2018). Mapping Surface Temperatures on a Debris-Covered Glacier with an Unmanned Aerial Vehicle. *Front. Earth Sci.*, *6*. doi: 10.3389/feart.2018.00064

Kraaijenbrink, P. D. A., Shea, J. M., Pellicciotti, F., de Jong, S. M., & Immerzeel, W. W. (2016). Object-based analysis of unmanned aerial vehicle imagery to map and characterise surface features on a debris-covered glacier. *Remote Sensing of Environment*, *186*, 581–595. doi: 10.1016/j.rse.2016.09.013

Krawczynski, M. J., Behn, M. D., Das, S. B., & Joughin, I. (2009). Constraints on the lake volume required for hydro-fracture through ice sheets. *Geophysical Research Letters*, *36*(10). doi: 10.1029/2008GL036765

Lampkin, D. J., Amador, N., Parizek, B. R., Farness, K., & Jezek, K. (2013). Drainage from water-filled crevasses along the margins of Jakobshavn Isbræ: A potential catalyst for catchment expansion. *Journal of Geophysical Research: Earth Surface*, *118*(2), 795–813. doi: 10.1002/jgrf.20039

Lampkin, D. J., Parizek, B., Larour, E. Y., Seroussi, H., Joseph, C., & Cavanagh, J. P. (2018). Toward Improved Understanding of Changes in Greenland Outlet Glacier Shear Margin Dynamics in a Warming Climate. *Frontiers in Earth*

Science, *6*. doi: 10.3389/feart.2018.00156
Lüthi, M. P., Ryser, C., Andrews, L. C., Catania, G. A., Funk, M., & Hawley, R. L. (2015). Heat sources within the Greenland Ice Sheet: Dissipation, temperate paleo-firn and cryo-hydrologic warming. *The Cryosphere*. doi: 10.5194/tc-9-245-2015
McGrath, D., Colgan, W., Steffen, K., Lauffenburger, P., & Balog, J. (2011). Assessing the summer water budget of a moulin basin in the Sermeq Avannarleq ablation region, Greenland ice sheet. *Journal of Glaciology*, *57*(205), 954–964. doi: 10.3189/002214311798043735
Minchew, B. M., Simons, M., Riel, B., & Milillo, P. (2017). Tidally induced variations in vertical and horizontal motion on Rutford Ice Stream, West Antarctica, inferred from remotely sensed observations. *J. Geophys. Res. Earth Surf.*, *122*(1), 2016JF003971. doi: 10.1002/2016JF003971
Mottram, R. H., & Benn, D. I. (2009). Testing crevasse-depth models: A field study at Breiðamerkurjökull, Iceland. *Journal of Glaciology*, *55*(192), 746–752. doi: 10.3189/002214309789470905
Nienow, P. W., Sole, A. J., Slater, D. A., & Cowton, T. R. (2017). Recent Advances in Our Understanding of the Role of Meltwater in the Greenland Ice Sheet System. *Curr Clim Change Rep*, 1–15. doi: 10.1007/s40641-017-0083-9
Nye, J. F. (1957). The distribution of stress and velocity in glaciers and ice-sheets. *Proceedings of the Royal Society of London. Series A. Mathematical and Physical Sciences*, *239*(1216), 113–133. doi: 10.1098/rspa.1957.0026
Phillips, E., Finlayson, A., & Jones, L. (2013). Fracturing, block faulting, and moulin development associated with progressive collapse and retreat of a maritime glacier: Falljökull, SE Iceland. *J. Geophys. Res. Earth Surf.*, *118*(3), 1545–1561. doi: 10.1002/jgrf.20116
Phillips, T., Rajaram, H., & Steffen, K. (2010). Cryo-hydrologic warming: A potential mechanism for rapid thermal response of ice sheets. *Geophysical Research Letters*, *37*(20). doi: 10.1029/2010GL044397
Poinar, K. (2015). *The influence of meltwater on the thermal structure and flow of the Greenland Ice Sheet* (Thesis).
Poinar, K., Dow, C. F., & Andrews, L. C. (2019). Long-Term Support of an Active Subglacial Hydrologic System in Southeast Greenland by Firn Aquifers. *Geophysical Research Letters*, *46*(9), 4772–4781. doi: 10.1029/2019GL082786
Poinar, K., Joughin, I., Das, S. B., Behn, M. D., Lenaerts, J. T. M., & van den Broeke, M. R. (2015). Limits to future expansion of surface-melt-enhanced ice flow into the interior of western Greenland. *Geophys. Res. Lett.*, *42*(6), 2015GL063192. doi: 10.1002/2015GL063192
Pope, A. (2016). Reproducibly estimating and evaluating supraglacial lake depth with Landsat 8 and other multispectral sensors. *Earth and Space Science*, *3*(4), 176–188. doi: 10.1002/2015EA000125
Porter, C., Morin, P., Howat, I., Noh, M.-J., Bates, B., Peterman, K., … Bojesen, M. (2018). *ArcticDEM.* Harvard Dataverse. doi: 10.7910/DVN/OHHUKH
Ryan, J. C., Hubbard, A., Stibal, M., Irvine-Fynn, T. D., Cook, J., Smith, L. C., … Box, J. (2018). Dark zone of the Greenland Ice Sheet controlled by distributed biologically-active impurities. *Nature Communications*, *9*(1), 1065. doi: 10.1038/s41467-018-03353-2
Ryan, J. C., Hubbard, A. L., Box, J. E., Todd, J., Christoffersen, P., Carr, J. R., … Snooke, N. (2015). UAV photogrammetry and structure from motion to assess calving dynamics at Store Glacier, a large outlet draining the Greenland ice sheet. *The Cryosphere*, *9*(1), 1–11. doi: 10.5194/tc-9-1-2015
Schoof, C. (2010). Ice-sheet acceleration driven by melt supply variability. *Nature*, *468*(7325), 803–806. doi: 10.1038/nature09618
Stevens, L. A., Behn, M. D., McGuire, J. J., Das, S. B., Joughin, I., Herring, T., … King, M. A. (2015). Greenland supraglacial lake drainages trig-

gered by hydrologically induced basal slip. *Nature*, *522*(7554), 73–76. doi: 10.1038/nature14480
Taylor, Z. J., Gurka, R., Kopp, G. A., & Liberzon, A. (2010). Long-Duration Time-Resolved PIV to Study Unsteady Aerodynamics. *IEEE Transactions on Instrumentation and Measurement*, *59*(12), 3262–3269. doi: 10.1109/TIM.2010.2047149
Todd, J., Christoffersen, P., Zwinger, T., Råback, P., & Benn, D. I. (2019). Sensitivity of a calving glacier to ice—ocean interactions under climate change: New insights from a 3-D full-Stokes model. *The Cryosphere*. doi: 10.5194/tc-13-1681-2019
van der Veen, C. J. (1998). Fracture mechanics approach to penetration of surface crevasses on glaciers. *Cold Regions Science and Technology*, *27*(1), 31–47. doi: 10.1016/S0165-232X(97)00022-0
van der Veen, C. J. (1999). Crevasses on glaciers. *Polar Geography*, *23*(3), 213–245. doi: 10.1080/10889379909377677
van der Veen, C. J. (2007). Fracture propagation as means of rapidly transferring surface meltwater to the base of glaciers. *Geophysical Research Letters*, *34*(1). doi: 10.1029/2006GL028385
Vaughan, D. G. (1993). Relating the occurrence of crevasses to surface strain rates. *Journal of Glaciology*, *39*(132), 255–266. doi: 10.3189/S0022143000015926
Weertman, J. (1973). Can a water-filled crevasse reach the bottom surface of a glacier. *IASH Publ*, *95*, 139–145.
Williamson, A. G., Banwell, A. F., Willis, I. C., & Arnold, N. S. (2018). Dual-satellite (Sentinel-2 and Landsat 8) remote sensing of supraglacial lakes in Greenland. *The Cryosphere*, *12*(9), 3045–3065. doi: https://doi.org/10.5194/tc-12-3045-2018
Williamson, A. G., Willis, I. C., Arnold, N. S., & Banwell, A. F. (2018). Controls on rapid supraglacial lake drainage in West Greenland: An Exploratory Data Analysis approach. *Journal of Glaciology*, 1–19. doi: 10.1017/jog.2018.8